

# Large-scale lithospheric stress field and topography induced by global mantle circulation

Bernhard Steinberger\*, Harro Schmeling, Gabriele Marquart

*Institut für Meteorologie und Geophysik, Johann Wolfgang Goethe-Universität, Feldbergstr. 47, 60323 Frankfurt am Main, Germany*

Received 3 July 2000; accepted 23 December 2001

## Abstract

Stresses in the lithosphere are one indication of processes in the Earth interior: here we present a calculation of large-scale lithospheric stresses caused by global mantle circulation. The mantle flow field is calculated based on density structures inferred from global seismic tomography. Predicted principal stress directions are compared to interpolations based on observed stresses. Agreement between predictions and observations is often good in regions where lithospheric stresses and mantle tomography are well constrained. Predicted magnitudes of scalar stress anomalies vary more strongly than predicted stress directions for various tomographic models. Hotspots preferentially occur in regions where calculated stress anomalies are tensile or slightly compressive. Results do not strongly depend on radial mantle viscosity structure, lithospheric rheology (viscous or elastic) or plate motion model. The model also predicts the directions of motion well for most plates; misfits in the predicted magnitudes can be explained qualitatively. Stress anomalies due to causes within the lithosphere (oceanic cooling with age, variations in crustal thickness, topography isostatically compensated at subcrustal levels) are also computed. Predicted stress directions in the absence of mantle flow can explain observations almost as well as mantle flow. Nevertheless, current models of mantle flow are largely in accord with interpolations of observed principal stress directions and the observed plate motions. © 2001 Elsevier Science B.V. All rights reserved.

**Keywords:** stress fields; lithosphere; mantle; hot spots; plate tectonics

## 1. Introduction

The dynamics of the Earth's interior is reflected in processes at the Earth's surface: due to mantle convection, lithospheric plates experience stresses

and move in response. It has been known for some time that the lithospheric stress field has a significant large-scale component, leading to preferential horizontal stress directions aligned over entire continents. Causes inside the lithosphere, such as variations in crustal and lithospheric thickness and density, as well as 'ridge push' and 'slab pull' forces have received attention early on, but more general models including the effects of global mantle flow [1] have been put forward as well [2,3]. The main idea that is formulated in these models and that is essentially also used

\* Corresponding author. Tel.: +49-69-798-24925;  
Fax: +49-69-798-23280;  
E-mail: steinber@geophysik.uni-frankfurt.de

here can be stated as follows: (1) the solid Earth (outside the core) can be rheologically divided into lithosphere ( $\approx$  top 100 km) and the viscous mantle beneath; the lithosphere is broken into about 14 plates that are approximately rigid, i.e. deform internally much less than the mantle beneath. (2) Internal density heterogeneities in the viscous mantle cause convective flow. (3) Mantle flow causes anomalies (formally defined below) of normal stress  $\tau_{rr}$  and tangential stresses  $\tau_{r\theta}$  and  $\tau_{r\varphi}$  at the base of the lithosphere. Tangential stresses can put the lithosphere under horizontal tension, compression or shear; anomalies of normal stress  $\tau_{rr}$  cause vertical displacements  $h_d$  of the lithosphere (dynamic topography) which induce downhill forces (defined below) that also cause tension or compression (Fig. 1).

For simplicity, we use a constant lithosphere thickness  $t_L = 100$  km, and a constant density of the lithosphere  $\rho_L = 3200$  kg/m<sup>3</sup> when computing stress anomalies caused by mantle flow. We always use  $\rho_w = 1020$  kg/m<sup>3</sup> for the density of ocean water, and  $g = 10$  m/s<sup>2</sup> for gravity. The downhill force per area is hence by definition:

$$\mathbf{f}_d = \Delta\rho \cdot \mathbf{g} \cdot t_L \cdot \nabla_h h_d \text{ with}$$

$$\Delta\rho = \begin{cases} \rho_L - \rho_w & \text{below water} \\ \rho_L & \text{otherwise} \end{cases} \quad (1)$$

where  $\nabla_h$  stands for the horizontal gradient. ‘Stress anomaly’ is defined as the tensor:

$$\tau = \begin{pmatrix} \tau_{rr} & \tau_{r\theta} \\ \tau_{r\theta} & \tau_{\theta\theta} \\ \tau_{r\varphi} & \tau_{\theta\varphi} \end{pmatrix} := \mathbf{T} - p\mathbf{I}$$

where  $\mathbf{T}$  is the total (in-situ) stress,  $p$  is the pressure of the reference Earth model which only depends on elevation (relative to the geoid) and  $\mathbf{I}$  is the unity tensor. The tensor elements are given in a coordinate system with basis vectors  $\mathbf{e}_r$ ,  $\mathbf{e}_\theta$  and  $\mathbf{e}_\varphi$  in radial (outward), southerly and easterly direction. Since only density variations (not total densities) enter our calculations, we directly obtain stress anomalies; the relation between total stress and density is formally the same as between stress anomaly and density anomaly. We also de-

fine a ‘horizontal stress anomaly tensor’:

$$\begin{pmatrix} \tau_{\theta\theta} & \tau_{\theta\varphi} \\ \tau_{\theta\varphi} & \tau_{\varphi\varphi} \end{pmatrix}$$

With a horizontal rotation of the coordinate system it can be diagonalized, i.e. brought into the form:

$$\begin{pmatrix} \tau_1 & 0 \\ 0 & \tau_2 \end{pmatrix}$$

$\tau_1$  and  $\tau_2$  are the principal, maximum and minimum horizontal stress anomalies, and for convenience we will refer to  $\tau_1 + \tau_2$  as the ‘scalar stress anomaly’; it shall be called ‘tensile’ if it has a positive value in lithosphere regions ‘under tension’, and ‘compressive’, if negative, in regions ‘under compression’.

Previously, the prediction of lithospheric stress anomaly based on mantle flow models was not particularly successful. The situation has, however, improved considerably during recent years. Because of an increased number of stress measurements [4,5] and improved interpolation methods [6], the actual large-scale stress field is better known. Also there has been progress in modelling: recent improvements in seismic tomography have given a more accurate knowledge of the Earth’s internal density heterogeneities and thus enable us to model mantle flow more realistically. In a recent paper [7] a mantle flow model based on seismic tomography [8] has been applied to predict dynamic topography in Africa, and it has been shown that the high elevations in southern Africa can be explained as dynamically supported. As dynamic topography and lithospheric stress due to mantle flow are closely related, it can be expected that a model that explains dynamic topography also gives a reliable prediction of the mantle flow contribution to lithospheric stresses. We therefore mainly use essentially the same tomographic model [8] here.

The main objective of this paper is thus to show that models of mantle flow are useful in explaining lithospheric stress anomalies if only a suitable density anomaly model is used. We intend to correct the impression left by previous work [3] that

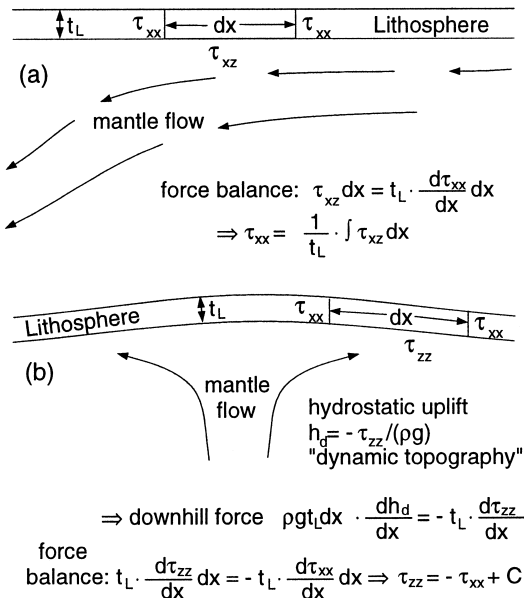


Fig. 1. Sketch illustrating in 2D cartesian geometry how lithospheric stresses are caused by mantle flow. (a) The lithosphere integrates shear stresses  $\tau_{xz}$  acting on its base. (b) Normal stresses  $\tau_{zz}$  at the base of the lithosphere cause 'dynamic topography' with elevated regions under tension, depressed regions under compression.

prediction of lithospheric stress based on mantle density anomalies is not particularly successful. Our modelling approach remains essentially the same as previously developed [2,3]. This objective is pursued through two lines of evidence: (1) the large-scale lithospheric scalar stress anomaly, i.e. the contribution due to mantle flow and due to isostatically compensated topography is computed and compared with the global distribution of hot-spots. If magma ascent is only possible through a lithosphere with tensile scalar stress anomaly, hot-spots should be predominantly located in those regions. (2) Directions of the minimum (i.e. most compressive) horizontal stress anomaly are computed and compared with an interpolated global stress map [6].

The calculations are done in two steps. In the first step, mantle flow and resulting sublithospheric stress anomalies acting at the base of the lithosphere are determined. This step is done for given surface velocity boundary conditions (such as a fixed surface, or plate-like surface velocities). No

further assumptions about the lithosphere (such as its thickness) are made. Here results on dynamic topography and free plate motions will be shown. This essentially repeats results from the literature, but with a new viscosity structure and (in the **EPSL Online Background Dataset**<sup>1</sup>) for a larger number of tomographic models, and comparison with the published results serves to verify our own computations. With 'free' plate motions we mean a set of plate rotation vectors such that for a prescribed geometrical shape of the plates no net torque acts on each plate (with plate boundary forces not included). How this condition is achieved will be discussed in Section 5. In the second step, normal and tangential surface tractions are used to predict stresses *within* the lithosphere. Additionally, stress anomalies due to isostatically compensated topography are also included. In this step, the stresses of the previous step are used as boundary conditions at the bottom of the lithosphere which is modelled as either elastic or highly viscous (i.e. viscosity is large compared to the underlying mantle). The upper boundary of the lithosphere is assumed shear stress free. This second step is explained first, in the following.

## 2. Calculation of stresses within the lithosphere due to forces acting at its base

This section essentially expresses the mechanism sketched in Fig. 1 in mathematical form in 3D spherical geometry: the stress anomaly is computed assuming force balance everywhere in the lithosphere, including stresses from the mantle at its base, from the side and due to downhill forces related to dynamic topography. How forces due to other topography can also be included will be introduced in Section 4. In the case of 'freely' moving plates we require per definition that the basal tractions add up to zero torque on each plate, and the force balance thus implies that also the forces acting on each plate from neigh-

<sup>1</sup> <http://www.elsevier.nl/locate/epsl>, mirror site: <http://www.elsevier.com/locate/epsl>

boring plates add up to zero torque, but plate boundaries are not stress-free locally in our model. In any other case, there will be a net torque acting on each plate from neighboring plates. Either an elastic or a highly viscous rheology is assumed in the lithosphere, with no lateral variations except (implicitly, since plates are allowed to move) at plate boundaries. This assumption implies that yield stresses integrated over the depth of the lithosphere are greater than the computed scalar stress anomaly multiplied with the assumed  $t_L$  everywhere except on plate boundaries in the case of non-zero plate motions. Comparison of our results shown below with lithospheric strength profiles [9] shows that this is probably the case for most regions. In the case of moving plates, it is also implied that plate boundaries behave perfectly plastic, with yield stresses integrated over the depth of the lithosphere being equal to the computed scalar stress anomaly times  $t_L$  at plate boundaries. Our results will show that ridges tend to be under tension and subduction zones under compression, as should be expected, with stress levels typically a few tens of MPa. Furthermore, if plates are allowed to move in our model, stress levels tend to drop at plate boundaries compared to a model with fixed plates. This is at least in qualitative agreement with what would be expected from a more realistic treatment with weak plate boundaries. Since a different approach, such as prescribing yield stresses at plate boundaries, would require a considerable modelling effort, and lithospheric rheology, particularly at plate boundaries, is still poorly known and an understanding of the plate-like behavior of the lithosphere is only beginning to emerge, we regard our approach as justified under present conditions. This subject has been previously discussed [1].

Because only long wavelengths  $\geq 1300$  km are considered, we approximate vertical lithospheric deflection to occur in the absence of flexural rigidity, i.e. we set in Eq. 1:

$$h_d = -\tau_{rr}/(\Delta\rho \cdot g) + h_{d,0} \quad (2)$$

and it hence follows from Eq. 1:

$$\mathbf{f}_d = \nabla_h \tau_{rr} \cdot t_L$$

$h_{d,0}$  is chosen such that  $h_d$  has a zero global mean value.

In the **EPSL Online Background Dataset**<sup>1</sup>, we estimate that flexural stresses can reach magnitudes similar to the stress anomalies calculated here for the shortest wavelengths included, but their relative magnitude gets smaller for longer wavelengths. Since the calculated stress pattern is predominantly very large-scale, we neglect flexural stresses and disregard variations of  $\tau_{\vartheta\vartheta}$ ,  $\tau_{\vartheta\varphi}$  and  $\tau_{\varphi\varphi}$  with depth in the lithosphere. With these approximations, we can express  $\tau_{\vartheta\vartheta}$ ,  $\tau_{\vartheta\varphi}$  and  $\tau_{\varphi\varphi}$  within the lithosphere in terms of  $\tau_{rr}$ ,  $\tau_{r\vartheta}$  and  $\tau_{r\varphi}$  at its base, using thin shell theory [10].

Firstly, stresses acting at the base of the lithosphere are expanded in spherical harmonics: following [1], we use hereby expansions:

$$\begin{aligned} \tau_{rr} &= \sum_{l=0}^{l_{\max}} \sum_{m=-l}^l \tau_{r,lm} \bar{Y}_{lm} \\ \tau_{r\vartheta} &= \sum_{l=0}^{l_{\max}} \sum_{m=-l}^l \tau_{p,lm} \frac{\partial \bar{Y}_{lm}}{\partial \vartheta} + \tau_{t,lm} \frac{1}{\sin \vartheta} \frac{\partial \bar{Y}_{lm}}{\partial \varphi} \\ \tau_{r\varphi} &= \sum_{l=0}^{l_{\max}} \sum_{m=-l}^l \tau_{p,lm} \frac{1}{\sin \vartheta} \frac{\partial \bar{Y}_{lm}}{\partial \varphi} - \tau_{t,lm} \frac{\partial \bar{Y}_{lm}}{\partial \vartheta} \end{aligned} \quad (3)$$

where  $\bar{Y}_{lm}$  are fully normalized spherical harmonics,  $l$  and  $m$  are spherical harmonic degree and order,  $\vartheta$  is co-latitude and  $\varphi$  is longitude.  $\tau_r$ ,  $\tau_p$  and  $\tau_t$  are called radial, poloidal and toroidal expansion coefficients of the sublithospheric stress anomaly tensor and are directly computed in the flow calculations [1]. In analogy, horizontal displacements or displacement rates (not including the rigid plate motions) of the lithosphere are expanded in terms of coefficients  $u_p$ , and  $u_t$ , or  $v_p$  and  $v_t$ . Then we can find equations that relate  $\tau_r$ ,  $\tau_p$  and  $\tau_t$  with  $u_p$  and  $u_t$ , or  $v_p$  and  $v_t$ :

$$\begin{aligned} v_p &= \left( \tau_r + \tau_p \frac{r_E}{t_L} \right) \frac{r_E}{\eta_L} \frac{1}{4l(l+1)-2} \\ v_t &= \frac{\tau_t r_E}{t_L} \frac{r_E}{\eta_L} \frac{1}{l(l+1)-2} \end{aligned} \quad (4)$$

for a highly viscous lithosphere:

$$u_p = \left( \tau_r + \tau_p \frac{r_E}{r_L} \right) \frac{r_E}{\mu_L} \frac{1}{4(l+1) \left( \left( \kappa_L + \frac{\mu_L}{3} \right) / \left( \kappa_L + \frac{4\mu_L}{3} \right) \right) - 2}$$

$$u_t = \frac{\tau_t r_E}{r_L} \frac{r_E}{\mu_L} \frac{1}{l(l+1)-2} \quad (5)$$

for an elastic one;  $\eta_L$ ,  $\mu_L = 0.721 \times 10^{11}$  Pa and  $\kappa_L = 1.134 \times 10^{11}$  Pa are viscosity, rigidity and incompressibility (also called bulk modulus) of the lithosphere,  $r_E$  is the Earth radius. These equations are derived in the **EPSL Online Background Dataset**<sup>1</sup>.

Indices  $lm$  are omitted in Eqs. 4 and 5. Subsequently, lithospheric strains or strain rates are computed from derivatives of displacements or displacement rates and, with the respective rheology, lithospheric stress components  $\tau_{\vartheta\vartheta}$ ,  $\tau_{\vartheta\varphi}$  and  $\tau_{\varphi\varphi}$  are calculated. Since we computed these three steps sequentially, the equations relating  $\tau_{rr}$ ,  $\tau_{r\vartheta}$  and  $\tau_{r\varphi}$  with  $\tau_{\vartheta\vartheta}$ ,  $\tau_{\vartheta\varphi}$  and  $\tau_{\varphi\varphi}$  were not explicitly derived: However, because the factors  $\eta_L$  for viscous rheology and  $\mu_L$  for elastic rheology cancel out, we know that the equations are (1) independent of viscosity for a viscous rheology and (2) similar for elastic and viscous rheology. Hence the calculated stress patterns for elastic and viscous lithosphere are very similar: lithospheric stress does not strongly depend on lithospheric rheology, as long as the assumptions made (uniform thickness, no faults, isotropic) are valid. If lithospheric rheology and thickness, and hence how effective a stress guide the lithosphere is, is not uniform, the stress pattern will change, however it is beyond the scope of this paper to investigate this effect.

### 3. Calculations of mantle flow and stresses acting at the base of the lithosphere

#### 3.1. Mantle density model

We use Grand's latest s-wave model (similar to [8]; the model and postscript figures are available via anonymous ftp://amazon.geo.utexas.edu) to infer density anomalies. We use a conversion factor  $(\delta\rho/\rho)/(\delta v_s/v_s) = 0.4$  from seismic velocity to

density anomalies that is close to what is inferred from both geodynamic models and laboratory data [11]. The conversion factor may vary with depth and given the different estimates proposed by various authors, uncertainties are probably a factor 2 or more [12]. Anomalies above 220 km are not included, as velocity anomalies in continental roots may be partly compositional in origin, and effects of oceanic lithospheric cooling are explicitly included, as explained in the **EPSL Online Background Dataset**<sup>1</sup>. Results for a number of other tomography models are included in the **EPSL Online Background Dataset**<sup>1</sup>, in order to enable a better judgement of which of our results depend on using this specific model and which ones do not.

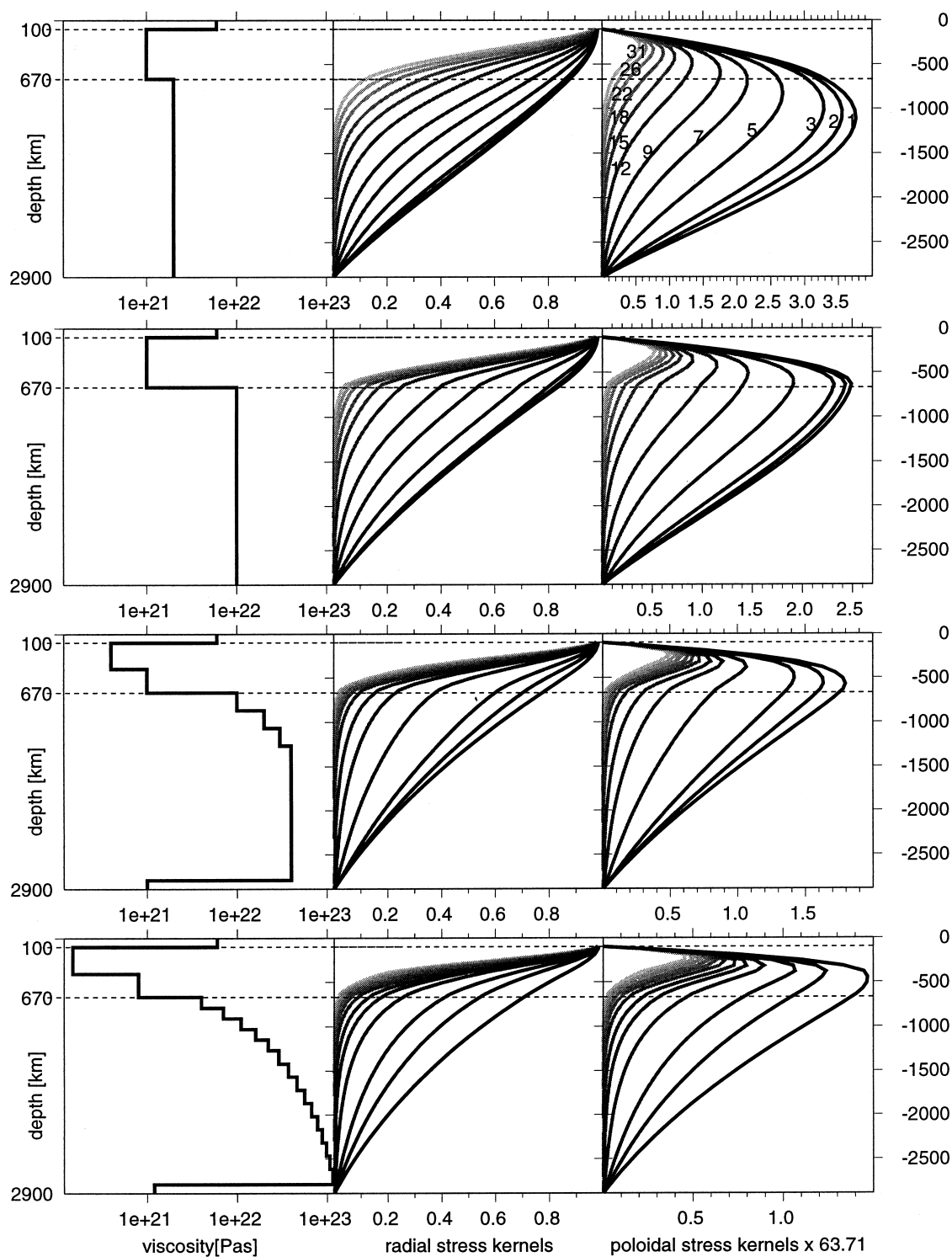
#### 3.2. Method of flow calculation

Following a usual approach, a linear viscous rheology is assumed in the mantle beneath the lithosphere, with viscosity varying in radial direction only. With this assumption it is possible to expand the equations of viscous flow in the mantle in spherical harmonics and thus reduce them to a set of ordinary differential equations that are solved separately for the poloidal and toroidal part and for each degree and order [1]. The method of calculating flow is the same as described previously [13]. In order to keep the model simple and the number of parameters low, incompressible flow without phase boundaries is assumed.

The stresses  $\tau_{rr}$ ,  $\tau_{r\vartheta}$  and  $\tau_{r\varphi}$  acting at the base of the lithosphere directly follow from the flow calculations. Only spherical harmonics up to  $l_{\max} = 31$  (corresponding to  $\approx 1300$  km wavelength) are considered. This is sufficient, as we are only concerned with long-wavelength lithospheric stress anomalies. Moreover, the resolution of tomographic models is lower than corresponding to degree  $l_{\max} = 31$  in many regions.

#### 3.3. Plate motion boundary condition

At the upper boundary, the two limiting cases considered are zero velocity, and free plate motions (discussed in Section 5). A third model, with plates moving at half the speed of free plate mo-



tions, is meant to represent an intermediate case; the fraction 0.5 used hereby has no particular significance. Which case is most appropriate depends on how plates move and how they are coupled to each other. If there is a lot of friction at the boundaries and the plates move slowly compared with the mantle beneath, the first case is more appropriate, if they glide past, above and beneath each other continuously and smoothly, the second case is more applicable.

Using the actual plate motions instead as a surface boundary condition is useful for calculating mantle flow fields, however it would mean applying forces to the plates that do not arise from mantle flow, and therefore would not give a good representation of lithospheric stresses. Comparison of predicted free and actual plate motions can however be used to assess how successful the models are. This is done below.

### 3.4. Viscosity structure

Fig. 2 shows a number of viscosity structures. Results shown in this paper were all computed for the *third* structure, with a 100-fold increase of viscosity with depth. Below the lithosphere and above 870 km depth, this viscosity model has been inferred from postglacial rebound [14]. A factor 100 viscosity increase is consistent with geodynamic models of the geoid and postglacial rebound [14–17]. Stresses were also computed for the other three viscosity structures, and it was found that the calculated stress patterns do not strongly depend on the viscosity structure used, although the viscosity increase with depth varies between a factor of 2 and around 700.

To illustrate the reason for this similarity, we have computed radial and poloidal stress kernels  $K_{r,l}$  and  $K_{p,l}$  and also display them in Fig. 2 for all four viscosity structures: in the case of zero plate motions, these stress kernels relate any density anomaly at depth  $d$  of degree and order  $lm$  to

the stress at the base of the lithosphere in 100 km depth implicitly accounting for an induced flow field of same degree and order:

$$\tau_{r,lm} = g \int \delta \rho_{lm}(r) K_{r,l}(d) dr$$

$$\tau_{p,lm} = g \int \delta \rho_{lm}(r) K_{p,l}(d) dr$$

A constant gravity  $g$  is assumed and  $\delta \rho_{lm}(r)$  are the spherical harmonic expansion coefficients of the density difference to the average mantle density as a function of depth. The kernels remain almost identical, if lithospheric viscosity is increased.

In the case of plate-like boundary conditions, as generally the case in this paper, stresses cannot be computed in terms of kernels, and toroidal stresses additionally arise. Nevertheless, the similarity of kernels for all four viscosity structures illustrates why computed stress patterns are rather independent of assumed viscosity structure.

### 3.5. Relative importance of radial and poloidal stresses

The stress kernels shown also illustrate and explain the relative importance of radial and poloidal stresses acting on the lithosphere. From Eqs. 4 and 5 we conclude that the relative magnitude of lithospheric stresses caused by radial versus poloidal stresses acting on its base can be approximated by the relative magnitudes of  $K_r$  and  $K_p \cdot r_E/t_L$ . Therefore, poloidal stress kernels in Fig. 2 have been multiplied by 63.71, corresponding to  $t_L = 100$  km. Except for the uppermost mantle, radial and poloidal stress kernels have a similar shape. For  $t_L = 100$  km, we expect that the effect of poloidal stress is about 2–4 times as large as the effect of radial stress; for the viscosity structure used in our further modelling (third row) it is expected to be about 2.5 times as large,

←  
Fig. 2. Vertical and poloidal stress kernels  $K_r$  and  $K_p$ , for a viscous incompressible mantle, for different viscosity structures and different spherical harmonic degrees. These are indicated by numbers in the upper right panel. In all other panels, kernels are plotted for the same degrees, with the same color scheme. In all four cases, a viscosity  $6 \times 10^{22}$  Pa s above 100 km depth was chosen, however kernels show very little dependence on assumed lithosphere viscosity.



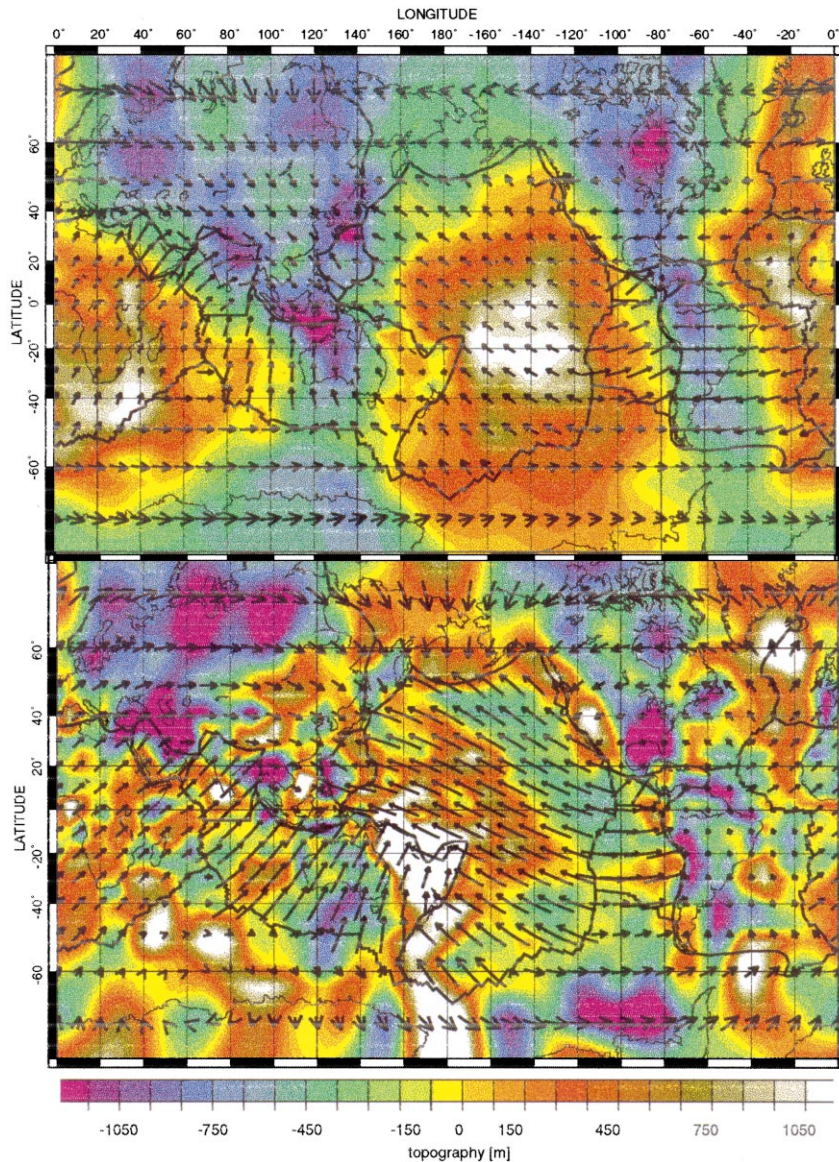


Fig. 3. Above: Predicted free plate motions and dynamic topography, calculated for plates moving at half the speed of free plate motions (i.e. half the speed that is shown). Plate boundaries are also shown here and in some of the following figures. Below: For comparison, NUVEL no-net-rotation [21] plate motions and residual topography are shown. In both panels topography is expanded up to spherical harmonic degree 31, and the same color scheme is used; an arrow length 222 km ( $2^\circ$  at the equator) corresponds to 1 cm/year; plate motions are expanded up to spherical harmonic degree 127.

with the effects of poloidal and radial stresses strongly correlated: this also implies that resulting stress patterns should be rather independent of the assumed value of  $t_L$ , although obviously stress magnitudes will depend on it.

In the actual stress calculations, which also al-

low for plate-like surface motions, the relative importance of radial and poloidal stresses, their strong correlation and the fact that the computed stress pattern does not strongly depend on  $t_L$ , are essentially verified. Toroidal stresses are found to play a less important role.



#### 4. Topography and stresses

Topography other than dynamic will also lead to stresses in the lithosphere: hereby we regard the actual topography  $h_{\text{obs}}$  (observed surface of the solid Earth, including ice cover, relative to its global mean value, not sea level), [18] as consisting of four parts: (a) dynamic topography  $h_{\text{d}}$ , (b) topography  $h_{\text{th}}$  due to cooling of the ocean lithosphere with age [19], (c) topography  $h_{\text{c}}$  isostatically compensated within the crust [20] and (d) any other topography (assumed to be isostatically compensated at subcrustal levels)  $h_{\text{sc}} := h_{\text{obs}} - h_{\text{d}} - h_{\text{th}} - h_{\text{c}}$ . For the given or assumed depths of isostatic compensation for parts (b), (c) and (d), an ‘equivalent normal stress’  $\tau'_{\text{rr}}$  is found, which can be used to compute lithospheric stresses  $\tau_{\vartheta\vartheta}$ ,  $\tau_{\vartheta\varphi}$  and  $\tau_{\varphi\varphi}$  in analogy to Section 2. Details are given in the **EPSL Online Background Dataset**<sup>1</sup>. Effects of continental lithospheric thickness variations on topography and stresses are not included.

The dynamic topography that is predicted from our model is shown in Fig. 3. Results do not strongly depend on the plate motion model used. How the specific plate motion model used here was obtained will be described in Section 5. In agreement with previous results [7], the predictions have a maximum amplitude of somewhat more than 1 km. The agreement between the variations in predicted dynamic and actually observed topography (or ‘residual topography’, as shown in Fig. 3, defined as  $h_{\text{res}} := h_{\text{obs}} - h_{\text{th}} - h_{\text{c}} = h_{\text{d}} + h_{\text{sc}}$ ) is quite good on the African continent. Even such detail features as the Congo basin are successfully predicted and in oceanic regions south of it, the predicted dynamic topography of  $> 1000$  m can help to explain the anomalously high elevations of the ocean floor. Predicted high elevations in the south central Pacific correspond to the ‘Pacific superswell’, and predicted low elevations between Australia and Antarctica correspond to the Australian–Antarctic discordance. In the North Atlantic around Iceland, a dynamic topography of 500–1000 m is predicted, however actual anomalous elevations in that region are even more than that. Continents other than Afri-

ca are generally below normal in both maps, however in many details the two maps do not agree well. The differences between the two maps may indicate parts of the topography that are isostatically compensated at subcrustal levels within the lithosphere. If this compensation occurs at great depth, which is especially possible within the continental lithosphere, it may lead to an important stress contribution. Here we assume that this compensation always occurs equally distributed in the mantle part of a 100 km thick lithosphere, because a more detailed treatment is beyond the scope of this paper. Further differences between predicted dynamic and residual topography occur because in some regions ocean floor ages are not known. This may be partly responsible for the anomalously high residual topography east of Australia (white color in Fig. 3, lower panel).

Although other topography may be larger than dynamic topography, lithospheric stress components  $\tau_{\vartheta\vartheta}$ ,  $\tau_{\vartheta\varphi}$  and  $\tau_{\varphi\varphi}$  arising from topography that is not dynamically maintained are generally (except in regions of very high altitude, particularly the Tibetan Plateau), comparatively small, for two reasons. Firstly, it is assumed here that the compensation depths of non-dynamic topography are smaller than the assumed lithospheric thickness. Thus, the equivalent normal stress  $\tau'_{\text{rr}}$  associated with a non-dynamic topography is smaller than the normal stress  $\tau_{\text{rr}}$  associated with the same amount of dynamic topography, i.e. arising from vertical displacements of the entire lithosphere. Secondly, from Eqs. 4 and 5 it follows that the horizontal lithospheric stress components are related to  $\tau_{\text{r}} + \tau_{\text{p}} \cdot r_{\text{E}}/l_{\text{L}}$ , and based on Fig. 2 we have estimated that the combined effect of these two terms is several times as large as the effect of dynamic topography alone.

#### 5. Free plate motions

The torque acting on plate  $i$  due to the forces discussed (with plate boundary forces not included) is:

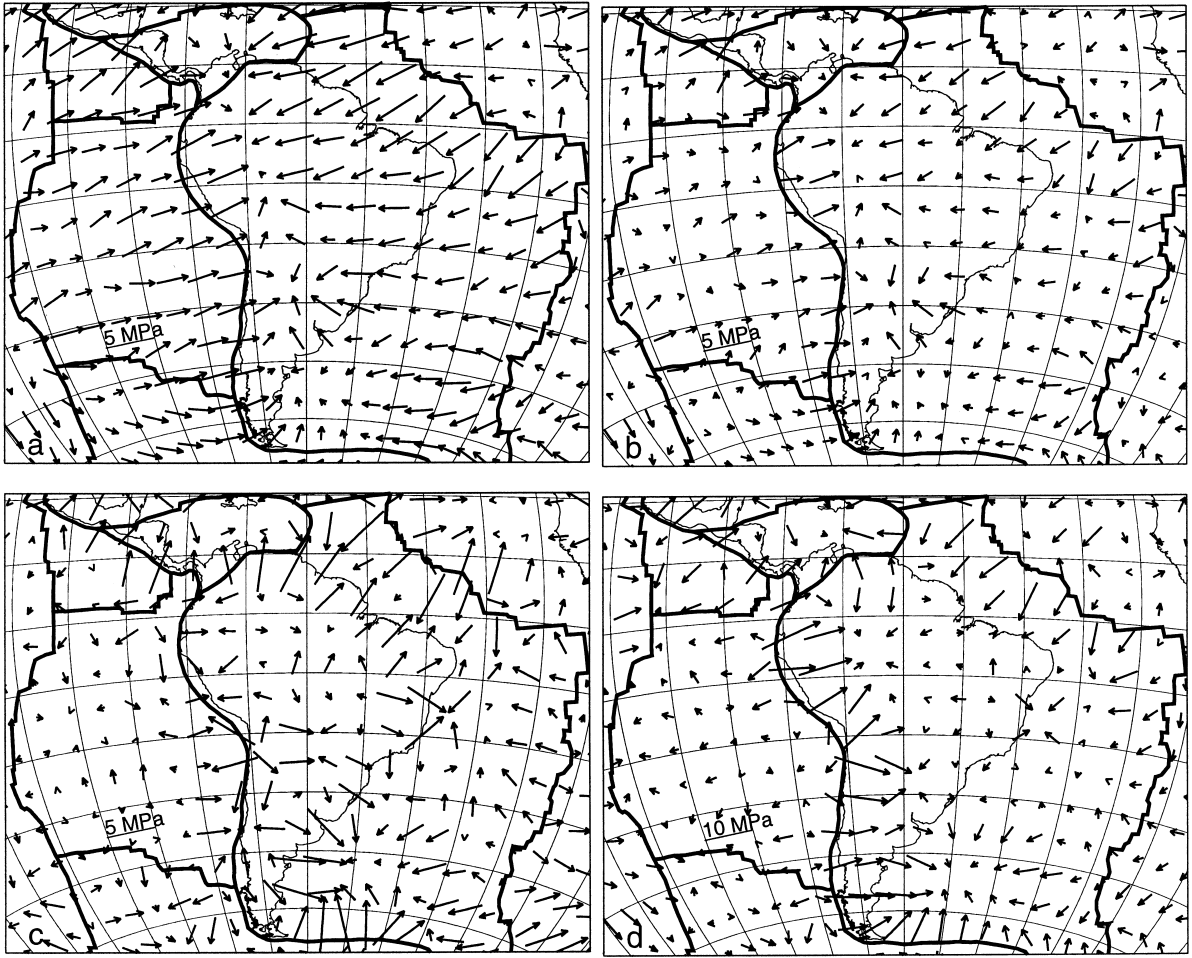


Fig. 4. Forces acting on the lithosphere in an area mainly covering the Nazca, Cocos, Caribbean and South American plates, plate boundaries are shown as thick black lines. (a) Shear stresses acting at the base. (b) Downhill force per area due to dynamic topography. (c) Force per area due to other topography. (d) Total force per area. (a)–(c) are for zero plate motions, (d) is for ‘free’ plate motions. 1 MPa corresponds to a  $2^\circ$  arrow length in (a)–(c),  $1^\circ$  in (d); grid spacing is  $10^\circ$ .

$$\mathbf{T}_i = \int \left[ \left( \frac{t_L}{r_E} \frac{\partial(\tau_{rr} + \tau'_{rr})}{\partial \vartheta} + \tau_{r\vartheta} \right) \mathbf{e}_\vartheta + \left( \frac{t_L}{r_E \sin \vartheta} \frac{\partial(\tau_{rr} + \tau'_{rr})}{\partial \varphi} + \tau_{r\varphi} \right) \mathbf{e}_\varphi \right] \times \mathbf{r} dA \quad (6)$$

where integration goes over the entire area of the plate. It is possible to find plate rotation vectors  $\boldsymbol{\omega}_i$ ,  $i=1, \dots, n$  such that the torque on each of the  $n$  plates vanishes. We call these the ‘free’ plate rotations. They can be computed by solving a

$3n \times 3n$  matrix equation. Details are given in the **EPSL Online Background Dataset**<sup>1</sup>.

The plate motions calculated in this way, as well as actual present-day plate motions [21] are shown in Fig. 3, both of them in a no-net-rotation reference frame. In most cases, predicted directions of plate motion agree well with observations. Differences in magnitude can be explained qualitatively. For example, the slab that pulls the Pacific plate is in nature attached to the plate, i.e. not separated by a zone of low viscosity as in the model; therefore ‘slab pull force’ and hence Pacific plate motion is underpredicted in our model. In

our model, the Nazca slab pulls both the Nazca and South American plate. Therefore our model overpredicts South American plate motion. The predictions, and the differences to actual plate motions, are similar to previous results [22,23].

## 6. Results for forces acting on the lithosphere

The forces acting on plates due to various causes are shown in Fig. 4 for a region mainly covering the Nazca and South American plate. This is a rather simple plate tectonic setting, bounded by two ridges with a subduction zone in the middle. Fig. 4a shows the basal shear stresses acting for zero plate motions: our mantle flow model features upwellings (corresponding to areas of high dynamic topography shown in Fig. 3) under the Pacific and Africa, and a downwelling under South America corresponding to a dynamic topography low. The latter is driven by positive density anomalies that apparently correspond to ancient subducted slabs. At the base of the lithosphere, we therefore calculate a flow from the upwellings to the downwelling that causes the shear stresses shown. The magnitude of shear stresses is typically a few MPa. Fig. 4b shows the downhill force per area due to dynamic topography. As expected from the stress kernels (Fig. 2), downhill forces generally have directions similar to basal shear stresses, and the magnitude of downhill force per area is on average somewhat less than half the magnitude of shear stress. The stresses shown in Fig. 4a,b correspond to what is known as ‘slab pull’, however the mechanisms are somewhat different. Because our model has no lateral viscosity variations, the positive density anomalies corresponding to subducted slabs do not pull at the end of plates in our model; rather the interaction comes about through basal tractions and downhill forces due to induced dynamic topography. These forces are distributed over the entire plate, in contrast to the classical slab pull. For that reason, a sharp distinction between slab pull and basal drag is not possible in our model.

Fig. 4c shows the force per area due to other topography: especially at the mid-Atlantic ridge, the effect of thermal thickening of the lithosphere

(‘ridge push’) is evident. The force per area has a magnitude similar to the downhill force per area, and is hence less important than the combined effect of mantle flow for the assumed viscosity depth distribution. Mainly on the East Coast of South America, the effect of the continent being elevated above the ocean floor is visible. The forces per area arising from this effect locally reach magnitudes larger than ridge push. The effect of the high elevations on the Altiplano can also be seen. Locally, this effect yields the highest forces per area, but globally there are only few areas with such high topography.

Fig. 4d shows the combined effect of all forces (Fig. 4a–c), with plates moving such that these forces act no net torque on the plate. In the classical notions this corresponds to including a basal drag to balance slab pull and ridge push. Since our analog to slab pull and ridge push also act distributed over the entire plate like basal drag, our model gives a good local force balance on the Nazca plate. For the South American plate, where our model features a strong downwelling beneath the plate, we can still distinguish between the mostly eastward forces to the west and the mostly westward forces to the east of the downwelling.

## 7. Results for lithospheric stresses

Fig. 5 shows that the pattern for the scalar stress anomaly is strongly dominated by long wavelengths and consists essentially of two regions in the Pacific and surrounding Africa under tension, surrounded by regions under compression. This dominance of long-wavelength degree two pattern arises, because (1) the tomographic model used already has a strong degree two component, (2) stress kernels are largest for the lowest spherical harmonic degrees and (3) the lithosphere integrates tangential stresses at its base, which also explains the high predicted scalar stress anomalies of about 100 MPa, substantially more than the shear stresses acting at the base of the lithosphere shown in Fig. 4, which were only a few MPa. Anomalies of normal stress contribute somewhat less than one third, i.e. around 30 MPa, corresponding to about 1 km dynamic topogra-

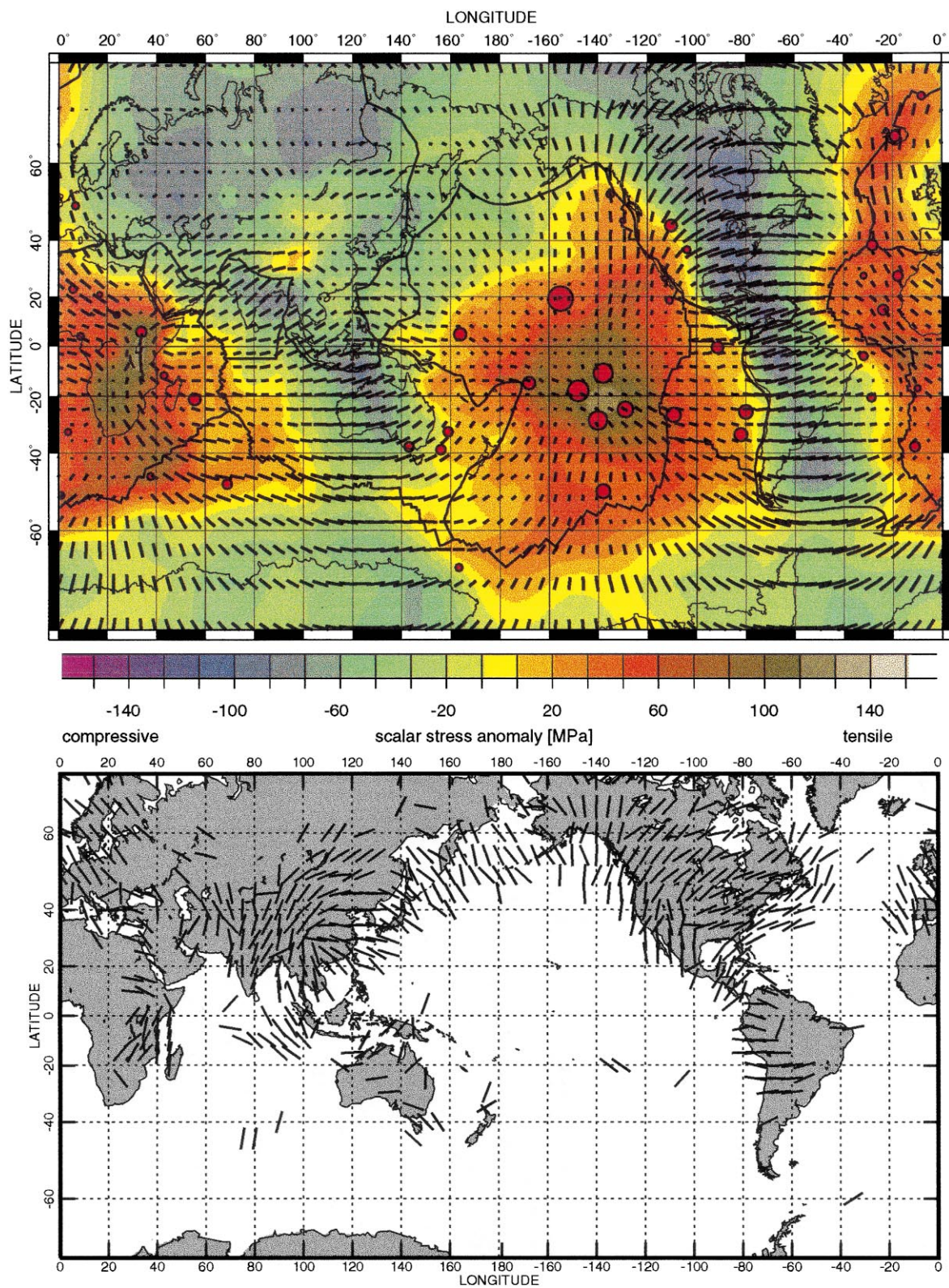




Fig. 5. Above: Calculated stress anomaly in the lithosphere: lines indicate the direction of the most compressive principal horizontal stress; length of lines is proportional to difference between the two principal horizontal stresses. At the equator,  $1^\circ$  length corresponds to 5 MPa difference, towards the poles correspondingly more, as the scale of the map, but not the scale for the stresses changes. Colors indicate the scalar stress anomaly as defined in the text. Also shown as red dots are locations of hotspots, with area of dots proportional to estimates of anomalous mass flux, according to our previous compilation [24], and plate boundaries. Calculation is done for an elastic lithosphere. Effects of mantle flow, cooling of the oceanic lithosphere and other topography are all included. Plates are moving at half the speed of ‘free’ motion. Below: a published interpolation [6] of the World Stress Map [4].

←

phy. The most tensile scalar stress anomalies are predicted in a region stretching north–south in East Africa, in agreement with location and orientation of where currently continental rifting occurs, and in a region of the south Pacific where a lot of intraplate volcanism occurs. Predicted stress anomaly levels due to mantle flow are probably too high in our model: because of strong vertical strength variations of the lithosphere, the stresses due to mantle flow that reach the surface are probably considerably lower than what is predicted here. Also, in cratonic regions the stresses will be distributed over a thicker lithosphere, leading to even lower stress anomalies. Principal stress directions should be less affected by this. A more detailed comparison of the scalar stress magnitudes predicted here with observations [4] is given in the **EPSL Online Background Dataset**<sup>1</sup>.

Also shown are locations of hotspots. They can be grouped in two clusters: in and around the Pacific, and centering on Africa. The regions of these clusters almost exactly agree with the two regions where tensile scalar stress anomalies are predicted: hotspots are completely absent from regions under strong compression.

Furthermore, the computed directions of maximum compressive principal horizontal stress are compared with an interpolation of observed stresses [6]: agreement tends to be best in regions where lithospheric stresses are well constrained and the resolution of seismic tomography is high (e.g. much of North America, Europe, East Asia). The mean azimuth error,  $31.41^\circ$ , is computed in the same way as in a previous, similar global model [25], i.e. with the weight given to each  $5 \times 5^\circ$  tile where the interpolated stress direction is shown in Fig. 5 only depending on its area, and independent of the calculated magnitude of stress

difference. The predicted directions of maximum compressive stress roughly form a radiating pattern around the two large-scale regions where tensile scalar stress anomalies are predicted in Southern Africa and the South Central Pacific, and a roughly ring-shaped pattern around the region in Eastern Europe where a compressive scalar stress anomaly is predicted.

In some parts of Asia, the predictions of Fig. 5 give a poor match to the observations: For the Tibetan region, the most compressive stress is in the N–S direction, whereas our model predicts the most tensile stress in that direction; in the Lake Baikal region, the predicted scalar stress anomaly is compressive whereas the observed stress anomaly is tensile. Disagreement is probably partly because the subducted lithosphere in East Asia pulls mainly at the Pacific plate, thus associated stress anomalies on the Asian continent are less compressive than in our model. Also, part of the isostatic compensation may occur at deeper levels than assumed here.

## 8. Discussion and conclusions

We have shown here a simple model to calculate stresses that are induced in the lithosphere by flow in the underlying viscous mantle. The results obtained are remarkably robust: they are similar for a variety of viscosity structures, lithospheric rheologies and plate motion models. The effects of mantle compressibility and phase boundaries, which were not included in the models shown here, was found to be rather small. The left two panels of Fig. 6 are meant to illustrate the robustness of the results: here either zero or free plate motions are assumed, and a viscous lithosphere

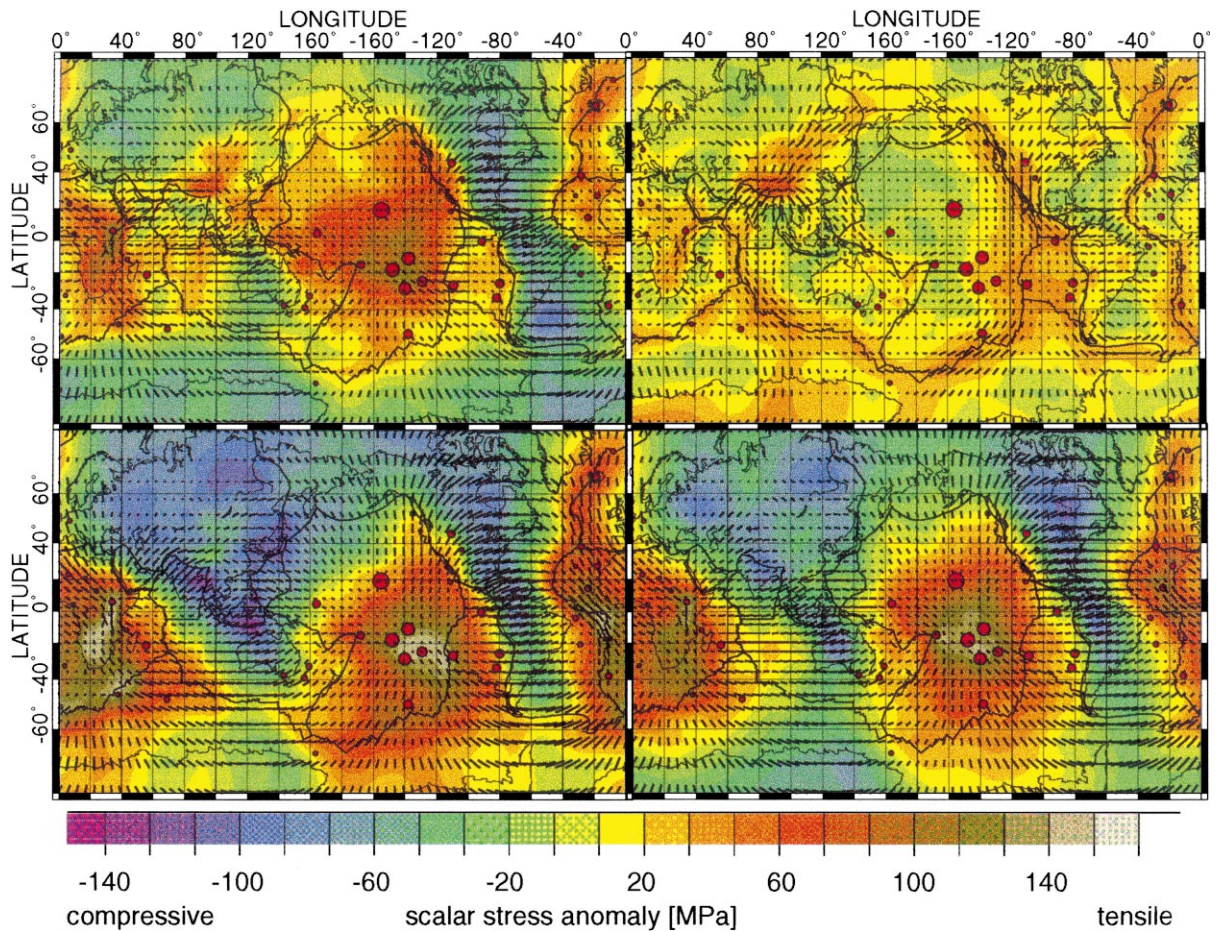


Fig. 6. Calculated magnitudes and directions of lithospheric stresses, and locations of hotspots. Calculation is done for a viscous lithosphere for free plate motions (top left) and zero plate motions (bottom left). Top right: Only stresses due to causes other than mantle flow are included, for zero plate motions, and assuming all topography is isostatically compensated within the lithosphere. Bottom right: Only stresses due to mantle flow are included, with plates moving at half the speed of free motion. Otherwise both models are the same as in Fig. 5. In the top right panel, the length of lines per stress difference is twice that of Fig. 5, in order to account for the smaller amplitudes of this model. For all other panels, the length scale of lines is the same as in Fig. 5.

rheology. Comparison with Fig. 5 shows that results do not critically depend on the assumed plate motion model or lithospheric rheology (viscous or elastic). The predicted patterns of both scalar stress anomalies and principal stress directions remain largely similar in all three cases. In the case of zero plate motions, absolute values of scalar stress tend to be larger, particularly along plate boundaries; in the case of free plate motions, they tend to be less, because the free plate motions are such as to release strongly compressive

sive or tensile stress anomalies along the boundaries. For example, in the top left panel of Fig. 6 the predicted scalar stress anomaly at the boundaries surrounding Africa tend to be of low magnitude (yellow color). The mean azimuth error of the predicted stress directions is  $36.41^\circ$  for free plate motions and  $29.98^\circ$  for zero plate motions, i.e. agreement is somewhat better if plates move at a lower speed than free plate motions: near many subduction zones, the observed directions tend to be orthogonal to the subduction zone. However

for free plate motions, the total force acting on each plate from neighboring plates adds up to zero, hence compressive stress anomalies orthogonal to subduction zones are, to a large part, removed in the model, such that the agreement with observed stress directions deteriorates. The comparison between predicted and observed stress directions is biased towards continents, whereas for a comparison of plate motions, oceans are most important; thus both kinds of data are complementary.

In the right two panels of Fig. 6 we compare results for lithospheric stress anomalies (1) computed with the assumption that all topography is isostatically compensated within the lithosphere (i.e. zero dynamic topography) and (2) arising from mantle flow only. Details of the first model are explained in the **EPSL Online Background Dataset**<sup>1</sup>. As expected based on Fig. 4, calculated scalar stress anomalies due to mantle flow (magnitudes about 100 MPa) tend to be larger than those computed under the second assumption (magnitudes about 30 MPa) for the assumed viscosity stratification. The stress anomalies calculated from mantle flow alone are hence similar to those calculated including all sources; the mean azimuth error, 31.19°, remains almost the same. On the other hand, if only other sources are included, the mean azimuth error is 30.37°, i.e. again almost the same as for the model shown in Fig. 5, but hotspots appear both in regions with tensile and with compressive stress anomalies calculated. Scalar stress magnitude predictions of this model are also compared to observations [4] in the **EPSL Online Background Dataset**<sup>1</sup>. Isostatic compensation may locally occur at greater depth than assumed here and stress levels due to mantle flow are likely overpredicted in our model, as was already discussed. Therefore stress anomalies due to topography isostatically compensated within the lithosphere likely play a greater role in reality than in our model shown in Fig. 5.

Results for predictions of lithospheric stress, free plate motions and dynamic topography for a number of other tomographic models are included in the **EPSL Online Background Dataset**<sup>1</sup> in order to allow a better assessment of the variations of results for different tomographic mod-

els. Directions of maximum compressive stress are similar for different tomographic models converted to mantle density, and the inferred stress patterns bear some resemblance to the interpolated principal stress directions [6]. On the other hand, predicted scalar stress anomalies show greater differences among various tomography models. For none of the other models is the agreement between areas where tensile stress anomalies are predicted and areas where hotspots cluster as good as for the Grand model, which yields tensile stresses of similar magnitude and areal extent for both the Pacific and Africa.

The predictions of ‘free’ plate motions (according to our definition in Section 5) and dynamic topography shown in Fig. 3, and in the **EPSL Online Background Dataset**<sup>1</sup> for other tomographic models, are similar to results that were obtained previously by other authors [7,22,23]. If there are forces acting on plate boundaries that would resist relative plate motions, actual plate motions should be smaller than predicted here. Our results in fact indicate that, if plate motions slower than calculated here are used, i.e. if such boundary forces are implied, the predicted stress directions match observations better than if we use the free plate motions calculated here. The reason why, despite this effect, the predicted plate motions are not generally faster than observed might be related to the fact that the Grand model has rather low amplitudes compared to other tomographic models.

One possible explanation for the relation between hotspot and stress distribution would be that magma ascent can only happen where the lithosphere is under tension, or slightly under compression. In other regions (such as under Labrador, where a plume has been suggested as the cause of anomalously high elevations [26] or under Baffin Bay and Kasachstan, where seismological observations may indicate the presence of a mantle plume; W. Spakman, personal communication) they may be present but not lead to surface volcanism. The absence of hotspots in most regions where past subduction took place and where stresses tend to be compressive may, however, also be caused by the disruption of plume conduits in the strong downward flow associated



with subduction [13], and by slabs cooling the core–mantle boundary.

At present, the understanding of relevant lithospheric rheology has not yet reached a stage of maturity; models of mantle convection with self-consistently generated plate tectonics are only beginning to emerge, as is evident from a number of papers in a recent monograph [27]. Therefore, we consider our simplifying assumptions appropriate. More realistic models remain future goals: in particular, improved models could feature lateral variations of mantle viscosity which may be several orders of magnitude, a more realistic treatment of plate boundaries, vertical layering of lithospheric strength and continental lithospheric thickness variations, including a possibly chemically distinct lithospheric root. Above all, such models could improve estimates of stress magnitude. We hope that our simple model can serve as kind of a ‘benchmark’ for such more sophisticated models. The results shown here are encouraging, given the simplicity of the model, and they clearly show that mantle flow is a viable explanation for a significant part of the large-scale lithospheric stress.

## Acknowledgements

We thank S. Grand for providing his tomographic model prior to publication, and P. Bird for interpolated stress directions (data and figures). Constructive reviews by P. Bird and two anonymous reviewers are appreciated. We also thank Paul Meijer for comments on a previous version of the manuscript. Most other figures were produced with GMT graphics [28]. *[RV]*

## References

- [1] B.H. Hager, R.J. O’Connell, A simple global model of plate dynamics and mantle convection, *J. Geophys. Res.* 86 (1981) 4843–4867.
- [2] Y. Ricard, L. Fleitout, C. Froidevaux, Geoid heights and lithospheric stresses for a dynamic Earth, *Ann. Geophys.* 2 (1984) 267–286.
- [3] W. Bai, C. Vigny, Y. Ricard, C. Froidevaux, On the origin of deviatoric stresses in the lithosphere, *J. Geophys. Res.* 97 (1992) 11729–11737.
- [4] M.L. Zoback, First and second-order patterns of stress in the lithosphere: the World Stress Map Project, *J. Geophys. Res.* 97 (1992) 11703–11728.
- [5] B. Mueller, V. Wehrle, K. Fuchs, The 1997 Release of the World Stress Map (available on-line at <http://www-wsm.physik.uni-karlsruhe.de/pub/Rel97/wsm97.html>), 1997.
- [6] P. Bird, Y. Li, Interpolation of principal stress directions by nonparametric statistics: global maps with confidence limits, *J. Geophys. Res.* 101 (1996) 5435–5443.
- [7] C. Lithgow-Bertelloni, P.G. Silver, Dynamic topography, plate driving forces and the African superswell, *Nature* 395 (1998) 269–272.
- [8] S.P. Grand, R.D. Van der Hilst, S. Widiyantoro, Global seismic tomography: a snapshot of convection in the Earth, *GSA Today* 7 (1997) 1–7.
- [9] G. Ranalli, *Rheology of the Earth*, Allen and Unwin, Boston, MA, 1987.
- [10] A.E.H. Love, *A Treatise on the Mathematical Theory of Elasticity*, Dover, New York, 1944.
- [11] S. Karato, Importance of anelasticity in the interpretation of seismic tomography, *Geophys. Res. Lett.* 20 (1993) 1623–1626.
- [12] A.M. Forte, R.L. Woodward, A.M. Dziewonski, Joint inversion of seismic and geodynamic data for models or three-dimensional mantle heterogeneity, *J. Geophys. Res.* 99 (1994) 21857–21877.
- [13] B. Steinberger, R.J. O’Connell, Advection of plumes in mantle flow: implications for hotspot motion, mantle viscosity and plume distribution, *Geophys. J. Int.* 132 (1998) 412–434.
- [14] K. Lambeck, P. Johnston, The viscosity of the mantle: evidence from analyses of glacial-rebound phenomena, in: I. Jackson (Ed.), *The Earth’s Mantle*, Cambridge University Press, Cambridge, 1998, pp. 461–502.
- [15] J.X. Mitrovica, A.M. Forte, Radial profile of mantle viscosity: results from the joint inversion of convection and postglacial rebound observables, *J. Geophys. Res.* 102 (1997) 2751–2769.
- [16] J.X. Mitrovica, Haskell [1935] revisited, *J. Geophys. Res.* 101 (1996) 555–569.
- [17] S.V. Panasyuk, B.H. Hager, A.M. Forte, Understanding the effects of mantle compressibility on geoid kernels, *Geophys. J. Int.* 124 (1996) 121–133.
- [18] National Geophys. Data Center, ETOPO-5 Bathymetry/Topography Data, Data Announc. 88-MGG-02, Natl. Oceanic and Atmos. Admin., US Department of Commerce, Boulder, CO, 1988.
- [19] R.D. Müller, W.R. Roest, J.-Y. Royer, L.M. Gahagan, J.G. Sclater, *A Digital Age Map of the Ocean Floor*, SIO Reference Series 93-30, Scripps Institution of Oceanography, 1996.
- [20] W.D. Mooney, G. Laske, G. Masters, CRUST 5.1: a global crustal model at  $5 \times 5^\circ$ , *J. Geophys. Res.* 103 (1998) 727–747.
- [21] C. DeMets, R.G. Gordon, D.F. Argus, S. Stein, Current plate motions, *Geophys. J. Int.* 101 (1990) 425–478.

- [22] Y. Ricard, C. Vigny, Mantle dynamics with induced plate tectonics, *J. Geophys. Res.* 94 (1989) 17543–17559.
- [23] C. Lithgow-Bertelloni, M.A. Richards, The dynamics of Cenozoic and Mesozoic plate motions, *Rev. Geophys.* 36 (1998) 27–78.
- [24] B. Steinberger, Plumes in a convecting mantle: models and observations for individual hotspots, *J. Geophys. Res.* 105 (2000) 11127–11152.
- [25] P. Bird, Testing hypotheses on plate-driving mechanisms with global lithosphere models including topography, thermal structure, and faults, *J. Geophys. Res.* 103 (1998) 10115–10129.
- [26] W.J. Morgan, Hotspot tracks and the opening of the Atlantic and Indian Oceans, in: C. Emiliani (Ed.), *The Sea*, vol. 7, *The Oceanic Lithosphere*, Wiley, New York, 1981, pp. 443–487.
- [27] M.A. Richards, R.G. Gordon, R.D. van der Hilst (Eds.), *The History and Dynamics of Global Plate Motions*, *Geophys. Monogr. Ser.* 121, Am. Geophys. Union, Washington, DC, 2000.
- [28] P. Wessel, W.H.F. Smith, New version of the Generic Mapping Tools released, *EOS Trans. Am. Geophys. Union* 76 (1995) 329.